

Elastic fields of quantum dots in subsurface layers

A. E. Romanov

A. F. Ioffe Physico-Technical Institute, Russian Academy of Sciences, 194021 St. Petersburg, Russia

G. E. Beltz and W. T. Fischer

Department of Mechanical and Environmental Engineering, College of Engineering, University of California, Santa Barbara, California 93106

P. M. Petroff and J. S. Speck^{a)}

Materials Department, College of Engineering, University of California, Santa Barbara, California 93106

(Received 22 August 2000; accepted for publication 11 January 2001)

In this work, models based on conventional small-strain elasticity theory are developed to evaluate the stress fields in the vicinity of a quantum dot or an ordered array of quantum dots. The models are based on three different approaches for solving the elastic boundary value problem of a misfitting inclusion embedded in a semi-infinite space. The first method treats the quantum dot as a point source of dilatation. In the second approach we approximate the dot as a misfitting oblate spheroid, for which exact analytic solutions are available. Finally, the finite element method is used to study complex, but realistic, quantum dot configurations such as cuboids and truncated pyramids. We evaluate these three levels of approximation by comparing the hydrostatic stress component near a single dot and an ordered array of dots in the presence of a free surface, and find very good agreement except in the immediate vicinity of an individual quantum dot. © 2001 American Institute of Physics. [DOI: 10.1063/1.1352681]

I. INTRODUCTION

Self-assembled quantum dots (SAQDs) have attracted substantial recent attention because they offer the potential for three-dimensional confinement of carriers and excitons and have “atom-like” electronic states.^{1,2} SAQD formation is commonly observed in large mismatch epitaxy of chemically similar materials.^{1,3} For example, the Stranski–Krastanow (SK) growth of InAs (or $\text{In}_x\text{Ga}_{1-x}\text{As}$) on GaAs first involves the growth of a ~ 1 to 2 monolayer thick “wetting layer” followed by coherent island formation.^{1,3} The SAQDs may be buried by the growth of the same materials as the underlying substrate. Subsequent growth of the strained composition on the buried dot template has been shown to lead to vertical stacking of dots provided that the thickness of the intervening layer (“spacer layer”) is in the order or thinner than the lateral dimensions of the dot.⁴

It is now clear that dot ordering is driven by the elastic field of subsurface stressors. Usually, these subsurface stressors are buried dots themselves (which give rise to vertical ordering).^{4–9} In group IV and III–V SAQD growth, the first dot layer does not demonstrate lateral order and subsequent layers show only vertical ordering (however, other subsurface stressors such as regular dislocation arrays¹⁰ or buried strained layers grown on patterned substrates¹¹ can initiate lateral ordering). Buried subsurface stressors lead to a modulation in the stress field and associated strain field on the growth surface which affects both adatom diffusion¹² and SK island nucleation rates.¹³

The strain fields caused by SAQDs strongly affect the electronic properties in the vicinity of the dots.^{14–19} Two

strain effects are predominant in the electronic properties of III–V semiconductors: changes in the conduction and valence band levels (deformation potentials) and local electric fields due to piezoelectric effects. The conduction band is only affected by the hydrostatic strain, often referred to as the dilatation or trace of the strain tensor. The valence levels can change both with hydrostatic and shear strain. For zinc blende structures, deviatoric strains (those strains which differ from pure hydrostatic strains) give rise to piezoelectrically induced electric fields.¹⁶ In the general case for zinc blende SAQDs, strain causes negligible change in the confined energy levels within the dots, however, the conduction and valence levels can be changed in the surrounding matrix. Further, strain can cause local piezoinduced electric fields within the dots and in the surrounding matrix.¹⁸ Additionally, strain can strongly modify the phonon frequencies within the dots in the surrounding material.¹⁷

Both for understanding ordering and the effects on electronic properties, it is important to determine the full elastic fields in the dots and surrounding matrix. The elastic fields depend on the lattice mismatch between the dot and matrix material, the elastic properties of both the dot and the matrix, the dot shape, and the position of dot with respect to the free surface. A complete solution of the elasticity problem in the most general case is not possible in closed analytical form. Independent of quantum dots, the general inclusion problem was extensively developed in the pioneering work of Eshelby^{20,21} and we address this approach in the next section. In the SAQD field, three main methods have been applied to determine the elastic strains and stresses, namely: (i) theory of inclusions based on the analytical solution of elasticity equations (“Eshelby-like” or related approaches),^{8,14,16,22–24} (ii) finite element methods (FEM),^{25–28} and (iii) atomistic

^{a)}Electronic mail: speck@mr1.ucsb.edu

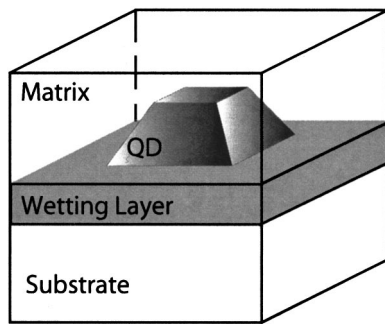


FIG. 1. General schematic of a buried quantum dot (QD). A wetting layer (WL) is shown, which may precede the formation of an island during the deposition of a dissimilar material onto a substrate. The island (quantum dot) is subsequently covered by additional matrix (substrate) material.

modeling.^{29–31} The theory of inclusions provides integral expressions for elastic fields which can be integrated in closed form only for the simplest inclusion shapes, such as cylinders or spheres. Even with the simplification of isotropic elasticity, the known application to quantum dots so far have neglected the effects of the free surface. FEM is very effective for particular cases but does not provide general solutions and is furthermore affected by the choice of boundary conditions for the modeling domain. Atomistic models require accurate interatomic potentials and are further restricted to small systems of atoms in comparison with dot sizes and the surrounding matrix.

In this article we apply two analytic approaches for SAQD mechanics which include the effect of the free surface and the dot shape and compare these results with FEM calculations. We concentrate on the far field solutions in the analytic approaches, as our main interests are related to dot ordering. However, we believe the analytic solutions are useful for determining the strain effects on the electronic structure of the matrix.

II. MODELING OF QUANTUM DOTS

From a continuum mechanics viewpoint, a quantum dot can be thought of as an inclusion of some prescribed shape embedded in a dissimilar matrix. Due to compositional differences which give rise to a lattice parameter mismatch or possibly a thermal expansion mismatch, the inclusion and surrounding matrix will be under a residual state of stress. Moreover, the inclusion may possess different elastic moduli from the matrix material. Assuming a linear elastic response, the resulting stress fields for such problems are very cumbersome and have only been worked out analytically for limited geometries, including cuboids^{32,33} and ellipsoids^{34,35} in infinite and semi-infinite domains. For the case of an ellipsoid in an infinite matrix, the solutions for this class of problems were originally developed by Eshelby in the 1950s.^{20,21}

Figure 1 shows a schematic based on experimental observations, in which a wetting layer initially forms when a material of new composition is deposited onto a substrate. After the wetting layer achieves several monolayers of thickness, an instability in growth leads to isolated island formation (future quantum dots).^{1,3,4} Currently, there are also indi-

cations that the wetting (transitional) layer may be much thicker (comparable with the dot height) and may possess different chemical composition than nucleating quantum dots. We do not address this issue in this article. Rather, we only consider the elastic field from the dot itself and do not consider the wetting. Although there is another controversy over the actual shape of quantum dots, it is clear from transmission electron microscopy (TEM) studies that they initially form as four-sided pyramids. Truncation of capped pyramids may be an illusion induced by strain fields observed by TEM. This possibility is supported by researchers reporting detailed contrast evidence in favor of sharp-capped pyramids.⁴ This controversy has implications for the present finite-element study. However, upper levels of pyramidal dots are relatively unstrained, and therefore would add little mechanical energy. For this reason, it is believed that the question of pyramid truncation will not have a pronounced effect on the conclusions to be obtained by modeling.

In this article we propose a number of simplified models to describe the elastic field surrounding a quantum dot. The simplest approach is to ignore the geometry of the dot altogether, and to regard it as a point source of dilatation of prescribed strength fV , where f represents the mismatch and V represents the volume of an “equivalent” dot, that is, the real dot that is being simulated by the point source. The parameter f represents the strain state developed in the quantum dot, relative to an equivalent volume of matrix material, if it were not constrained by the matrix; for example, if a dot with lattice parameter a_d is deposited onto a substrate surface with lattice parameter a_s , the misfit strain f is taken as $(a_s - a_d)/a_d$. When the island is subsequently surrounded by matrix material, the constraint is uniform in three directions; hence the misfit strain components become $f\delta_{ij}$. Similarly, a thermal expansion mismatch gives rise to such a dilatational self-strain (also known in the literature as the stress-free strain or the “eigenstrain”), so all sources of misfit may be incorporated into the single parameter f . Of course, such an approach is expected to yield expressions that break down in the general vicinity of the dot.

A powerful method for the solution of a broad spectrum of problems in elasticity derives from a consideration of point forces applied at some point in the elastic body.^{36,37} If the response of a body to a point force (i.e., the Green’s function) is known, the deformation caused by any distribution of forces can be obtained by superposition. For example, the displacement field caused by a single point force applied anywhere in an infinite elastic solid may be determined quite straightforwardly from the field equations of elasticity.³⁷ If the body is finite, as in the case of a semi-infinite space, a traction-free boundary condition must be satisfied, thereby giving a corrective term to the displacement field for an infinite solid.

In the case of a point source of expansion, three mutually perpendicular pairs of forces (each pair consists of a dipole of opposing forces of magnitude P , separated by a distance d along their mutual line of action) may be used (see Fig. 2). If one considers a cube of volume $V = d^3$, the average stress in the cube is P/d^2 , which in turn can be related to the strains arising from the misfit f via Hooke’s law. Apply-

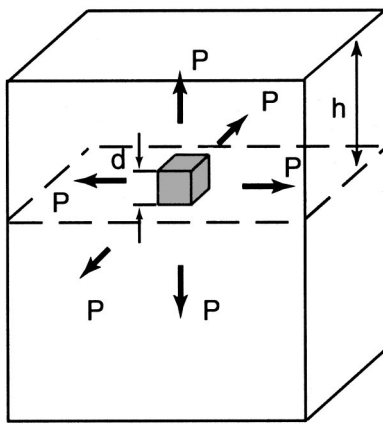


FIG. 2. Point source of dilatation at distance h from a free surface, represented as a cube with infinitely small dimension d . Three force dipoles P are applied to the faces of this cube.

ing such an argument to an isotropic medium, one may arrive at the relation $Pd = [2(1 + \nu)\mu / (1 - 2\nu)]fV$, where μ is the material shear modulus and ν is Poisson's ratio. By taking the limit as $d \rightarrow 0$, maintaining Pd constant, the complete elastic field for a point of expansion of a given strength may be identified. Mindlin³⁸ and Mura^{34,35} have provided the appropriate expressions for such point sources, not only for a generally anisotropic medium, but also for a point source located in a semi-infinite, isotropic medium. The primary advantage with this method is that the expressions are compact, especially for the case of an isotropic medium, as illustrated in Sec. III A.

The next level of complexity would be to idealize the quantum dot as an inclusion of some simplified shape, such as spherical, ellipsoidal, or cuboidal. Mura^{34,35} has developed expressions for an ellipsoidal inclusion in a half-space in an extension of the point-source analysis described above by integrating the appropriate Green's function over the volume of the inclusion. Chiu^{32,33} has provided similar results, but for a cuboidal inclusion embedded in a semi-infinite medium. Despite these relatively simple shapes, closed form solutions are only possible for the ellipsoid when at least two of the semiaxes are identical, as demonstrated below. In the example to be discussed in Sec. III B, an oblate spheroid (an ellipsoid with semiaxes $a_1 = a_2 > a_3$), a depth h from the surface, will be considered, either alone or as an ordered array of spacing l (see Fig. 3). Although the stress expressions are more cumbersome than for the point sources of dilatation (as given below in Sec. III B), the advantage is that a more realistic idealization of the quantum dot geometry is achieved, and in such a way that the effect of the aspect ratio of the dot may be efficiently evaluated.

For the case of quantum dots with extreme aspect ratios, for example, a relatively flat square or "penny-shaped" quantum dot, the stress field may be approximated as that due to an appropriately shaped prismatic dislocation loop, the stress fields for which are well-known. As the quantum dot deviates from an extreme aspect ratio, this method still works, because the shape may be represented by an array of prismatic dislocation loops. Li³⁹ and Gutkin and coworkers^{40,41} have exploited this equivalence for determin-

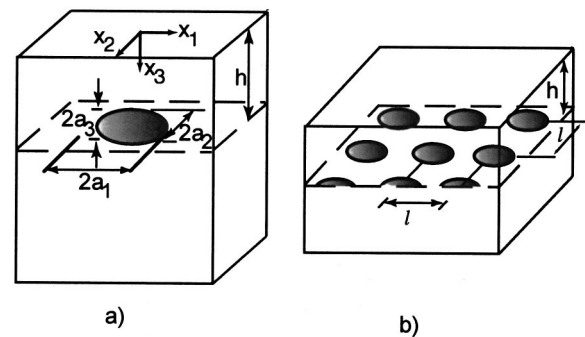


FIG. 3. Ellipsoidal inclusions used to model quantum dots. (a) An isolated ellipsoidal inclusion at distance h from the surface, with semiaxes a_1 , a_2 , and a_3 in the corresponding coordinate directions. (b) A rectangular array of the same ellipsoidal inclusions, with periodicity l in the lateral coordinate directions.

ing the stress fields around various inclusion shapes, albeit in a different context from quantum dot behavior. For the sake of brevity, we do not outline this method in this article.

The final level of complexity undertaken in this article is to evaluate the complete stress field in the vicinity of a cuboidal or trapezoidal inclusion via the finite element method (FEM). In other words, we model the geometries similar to that of Fig. 1, excluding the wetting layer. The FEM models can easily be expanded to include the wetting layer (see, for example, Ref. 28); however, we do not undertake that here since the primary goal is to make comparisons with the quantum dot models based on point sources and ellipsoidal inclusions mentioned earlier. For a typical trapezoidal inclusion within a matrix unit cell, elastic solutions may be approximated using a finite element mesh comprising one quadrant of an arbitrarily deep matrix unit cell, with appropriate boundary conditions imposing symmetry at the lateral faces (see Sec. III C). The primary advantage with this method is that more details concerning the stress field may be revealed, especially near the sharp corners of the inclusion. The FEM technique can readily include elastic anisotropy combined with different elastic constants for the matrix and the dot. The disadvantage is that a mesh must be created for each dot geometry, and the size of the matrix mesh must be made arbitrarily large in order to compare these results with those of the point source or the inclusion.

To simulate this residual strain in the model presented here, perfect bonding is assumed, and strains are imparted by a "phantom" thermal expansion mismatch between the inclusion and the matrix. Of course, in the system simulated, thermal expansion mismatch may or may not be a significant effect. However, since the effect of introducing such a differential expansion is to change the zero-stress lattice size for both materials, there is no analytical difference between differential strains induced by lattice mismatch, and those induced by thermal expansion mismatch.

III. ELASTIC SOLUTIONS FOR SUBSURFACE QUANTUM DOT STRESSORS

A. Point source of dilatation

For the case of a single point source of expansion located a distance h from the surface, the displacement field is

given by Mura.^{34,35} We have differentiated that expression to obtain strain through the relation $\varepsilon_{ij} = \frac{1}{2}(u_{i,j} + u_{j,i})$ and subsequently used Hooke's law, $\sigma_{ij} = 2\mu(\varepsilon_{ij} + [\nu/(1-\nu)]\delta_{ij}\varepsilon_{kk})$ to obtain the result

$$\begin{aligned} \sigma_{ij} = & \frac{\mu f V (1 + \nu)}{2\pi(1-\nu)} \left[-\left(\frac{1}{R_1}\right)_{,ij} - x_3 \left(\frac{2}{R_2}\right)_{,3ij} \right. \\ & + (3-4\nu)(\delta_{3i} + \delta_{3j} - 1) \left(\frac{1}{R_2}\right)_{,ij} - \delta_{3j} \left(\frac{1}{R_2}\right)_{,3i} \\ & \left. - \delta_{3i} \left(\frac{1}{R_2}\right)_{,3j} + \nu \delta_{ij} \left(\frac{4}{R_2}\right)_{,33} \right], \end{aligned} \quad (1)$$

where, as before, μ is the shear modulus, ν is the Poisson's ratio, f is the mismatch, V is the dot volume, and δ_{ij} is the Kronecker delta. The quantities R_1 and R_2 are given by $\sqrt{x_1^2 + x_2^2 + (x_3 - h)^2}$ and $\sqrt{x_1^2 + x_2^2 + (x_3 + h)^2}$, respectively. The notation $(\)_{,i}$ indicates $\partial/\partial x_i(\)$ while repeated indices are summed from 1 to 3. The use of a finite volume in these formulas is an approximation, as discussed in the previous section, since the expressions really derive from differential equations and are exact for the case of a vanishingly small inclusion. These expressions are expected to only yield realistic results when considering target distances compared with the characteristic length of the quantum dot, for example, the stresses at the surface for cases where the quantum dots are buried sufficiently beneath the surface.

In order to graphically illustrate the stress distribution near a quantum dot and to facilitate comparisons with other, more precise representations of the stress field, we use the trace of the stress tensor σ_{kk} rather than individual components. This component is the key quantity for calculating the interaction energy between a quantum dot and an adatom on the surface, and thus the driving force for adatom diffusion at the surface. The trace is related to the pressure through the relation $p = -\frac{1}{3}\sigma_{kk}$ and is given by

$$\begin{aligned} \sigma_{kk} = & \frac{2\mu f V (1 + \nu)^2}{\pi(1-\nu)} \left(\frac{1}{R_2}\right)_{,33} \\ = & \frac{2\mu f V (1 + \nu)^2}{\pi(1-\nu)} \frac{[2(x_3 + h)^2 - x_1^2 - x_2^2]}{[x_1^2 + x_2^2 + (x_3 + h)^2]^{5/2}}. \end{aligned} \quad (2)$$

The local dilatation, ε_{kk} , is given by $-p[3(1-2\nu)/2\mu(1+\nu)]$, where the quotient of elastic constants is the inverse of what is referred to as the bulk modulus. The dilatation is of interest due to its effect on the electronic band structure in and near the quantum dot¹⁶ and on dot nucleation and growth due to the surface diffusion.¹² We note that in Eqs. (1) and (2), all terms containing R_1 comprise the solution for the case when the point source is embedded in an infinite medium, and the terms with R_2 represent the correction due to the presence of the free surface. Hence $\sigma_{kk} = 0$ for an infinite solid but not for the semi-infinite solid. The effect of the free surface on the dilatation field of various inclusions was studied in greater detail by Michel *et al.*^{42,43}

For the case of an ordered array of quantum dots (see Fig. 3), the stress field can be obtained by summing Eq. (1)

or Eq. (2) over all dots. For a square array of dots of spacing ℓ , the trace of the stress tensor at all locations is given by

$$\begin{aligned} \sigma_{kk} = & \frac{2\mu f V (1 + \nu)^2}{\pi(1-\nu)} \\ & \times \sum_{i=-\infty}^{\infty} \sum_{j=-\infty}^{\infty} \frac{[2(x_3 + h)^2 - (x_1 - i\ell)^2 - (x_2 - j\ell)^2]}{[(x_1 - i\ell)^2 + (x_2 - j\ell)^2 + (x_3 + h)^2]^{5/2}}, \end{aligned} \quad (3)$$

where h represents the depth of the planar array of dots. The double sum represented in Eq. (3), to our knowledge, has no analytic representation; however, it can be numerically evaluated by replacing ∞ with some suitably large integer.

B. Ellipsoidal dilated inclusion

As shown by Mura,^{34,35} the stress field for an ellipsoidal inclusion in a half space can be obtained by integrating the displacement field that gave rise to Eq. (1) over the domain

$$\frac{x_1'^2}{a_1^2} + \frac{x_2'^2}{a_2^2} + \frac{(x_3' - h)^2}{a_3^2} \leq 1, \quad (4)$$

where a_1 , a_2 , and a_3 denote the semiaxes of the ellipsoid along the respective coordinate directions, and h denotes the depth of the center of the ellipsoid from the surface. For points exterior to the inclusion, the stress components take the form

$$\begin{aligned} \sigma_{ij} = & \frac{\mu f V (1 + \nu)}{2\pi(1-\nu)} \left[-\psi_{,ij} - 2x_3 \phi_{,3ij} + (3-4\nu) \right. \\ & \left. \times (\delta_{3i} + \delta_{3j} - 1) \phi_{,ij} - (\delta_{3i} + \delta_{3j}) \phi_{,ij} + 4\nu \delta_{ij} \phi_{,33} \right], \end{aligned} \quad (5)$$

where

$$\psi = \frac{3}{4} \int_{\lambda}^{\infty} \frac{1 - \left(\frac{y_1^2}{a_1^2 + s} + \frac{y_2^2}{a_2^2 + s} + \frac{y_3^2}{a_3^2 + s} \right)}{\sqrt{(a_1^2 + s)(a_2^2 + s)(a_3^2 + s)}} ds \quad (6)$$

with

$$\frac{y_1^2}{a_1^2 + \lambda} + \frac{y_2^2}{a_2^2 + \lambda} + \frac{y_3^2}{a_3^2 + \lambda} = 1 \quad (7)$$

and

$$\phi = \frac{3}{4} \int_{\lambda}^{\infty} \frac{1 - \left(\frac{z_1^2}{a_1^2 + s} + \frac{z_2^2}{a_2^2 + s} + \frac{z_3^2}{a_3^2 + s} \right)}{\sqrt{(a_1^2 + s)(a_2^2 + s)(a_3^2 + s)}} ds \quad (8)$$

with

$$\frac{z_1^2}{a_1^2 + \lambda} + \frac{z_2^2}{a_2^2 + \lambda} + \frac{z_3^2}{a_3^2 + \lambda} = 1. \quad (9)$$

The coordinate transformation for y_i and z_i is defined such that

$$\begin{aligned} x_1 = y_1 = z_1, \quad x_2 = y_2 = z_2, \\ x_3 = y_3 + h = z_3 - h. \end{aligned} \quad (10)$$

We have found that the integrals represented by Eqs. (6) and (8), which require the roots of Eqs. (7) and (9), respectively, for λ can be obtained analytically in terms of elementary functions if at least two of the semi-axes a_1 , a_2 , and a_3 are equal. Accordingly, we have chosen $a_1 = a_2 = 3a_3$ for the example results to be displayed below. The volume of such an inclusion is given by $V = 12\pi a_3^3$. Here, the ellipsoid looks round when viewed from the surface, but its thickness in the x_3 direction may be varied for a basic study of the effect of aspect ratio on the stress field.

As with the point sources discussed in the previous section, the stress field associated with an ordered array of ellipsoidal inclusions may be straightforwardly determined by summing Eq. (5) over all dot positions, in the precise manner as shown for Eq. (3).

C. Cuboidal and trapezoidal inclusions (finite-element method)

The finite element method is best suited to modeling of elastic fields associated with inclusion geometries more complex than ellipsoids. For the creation of the meshes, we used a widely available finite-element analysis software application, ABAQUS. ABAQUS permits the closely controlled generation of finite-element meshes through the use of input files containing complete instructions for node-by-node and element-by-element mesh specification, along with imposition of boundary conditions. For a typical trapezoidal inclusion within a matrix unit cell, elastic solutions may be approximated using a finite-element mesh comprising one quadrant of an arbitrarily deep matrix unit cell, with appropriate boundary conditions imposed at the lateral faces. Meshes generated included one quarter of a cuboidal or trapezoidal inclusion, at various depths, embedded in a matrix of identical elastic properties (see Fig. 4). The mesh uses eight-node linear brick elements with $\mu = 1$ and $\nu = 1/3$. The mismatch strain f was taken as unity by identifying the thermal expansion strain in the inclusion, $\alpha\Delta T$, with unity. In this fashion, any value of f may be considered due to linearity.

Depths of the inclusion centroid varied between $3a_3$ and $12a_3$, for direct comparison with point source and ellipsoidal inclusion results (recall a_3 denotes the half-height of the ellipsoidal inclusion). The FEM domain has lateral dimensions of $6a_3$ in each direction, appropriate for an interinclusion spacing of $12a_3$. For the inclusion shape, truncation angles of 0° and 30° were used (see inset, Fig. 4). The former we refer to as a cuboid, and the latter a trapezoid. The lateral dimension of the inclusion is determined by enforcing that its volume is identical to that of an ellipsoidal inclusion with the same height, $2a_3$. With the volume and thickness fixed, there is an inclusion base dimension associated with each choice of truncation angle α . The inclusions consist of 125 evenly spaced elements, while the matrix elements include a dimensional bias such that they become larger near the far walls, but smaller again as they approach the free surface.

Two general types of cases were investigated. The simplest was the case of a single inclusion submerged in a semi-infinite half space. The second type of case involved an infinite two-dimensional array of submerged inclusions. The

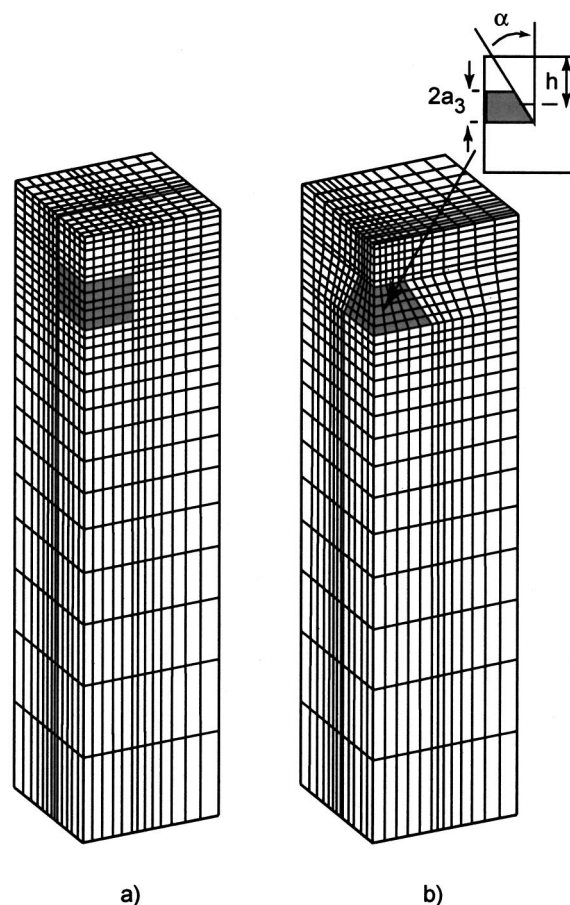


FIG. 4. Mesh used in finite element calculations of elastic fields for (a) cuboidal ($\alpha = 0^\circ$), and (b) trapezoidal ($\alpha = 30^\circ$) quantum dot configurations. One quarter of the domain is needed in this calculation due to fourfold symmetry about the longitudinal axis. The inset shows the critical parameters used to describe the geometry of the quantum dot, including the truncation angle α . The depth h is always taken from the centroid of the quantum dot, and the lateral dimension of the dot is chosen such that its volume is the same as an ellipsoidal dot discussed in Fig. 3.

latter is more difficult to approximate using analytical approaches because of the sum given by Eq. (3). Somewhat surprisingly, however, the periodic case presents fewer obstacles to the finite-element approach than does the singular case.

For models of a single trapezoidal inclusion submerged in a semi-infinite half space, we insist that normal displacement must vanish at the two walls in contact with the inclusion, consistent with the division of the inclusion (and matrix unit cell) into symmetric quadrants.

The bottom surface is constrained similarly, although the type of condition imposed at the bottom is less important than the depth, which should be sufficiently large to be considered “far field.” It must be admitted that the use of the same boundary condition as that imposed at the lateral walls in contact with the inclusion does, in fact, give rise to a similar periodicity in depth, which is not intended. However, with a large dimension of matrix below the inclusion, the effect of this depth image stress field will be minimal. We could just as easily use a fully encastered or free boundary condition (or any other that would result in a traction-free far field surface condition), so long as the depth is large and

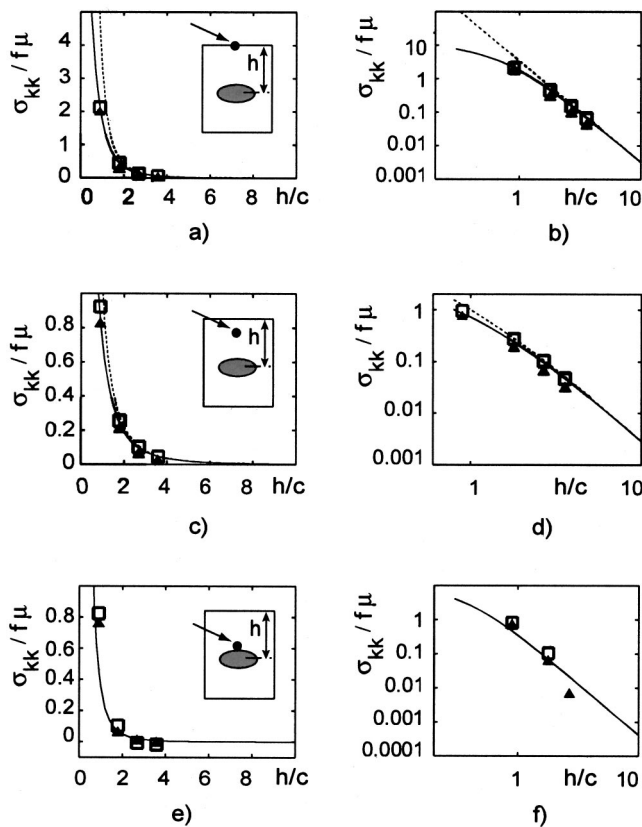


FIG. 5. Plots of stress σ_{kk} versus dot depth, for an isolated dot, for the various models considered in this article. In all cases, the solid line is for an ellipsoidal inclusion ($a_1 = a_2 = 3a_3$); the dashed line is for a point source of dilatation, the open square is for the FEM model of the cuboid, and the closed triangle is for the FEM model of the trapezoidal dot. In (a) and (b) we show the trace of the stress tensor at the surface directly above the dot. In (c) and (d) we show the stress at the surface, evaluated at depth $c/2$ (where c is related to the volume of the dot by $c = V^{1/3}$), above the dot. In (e) and (f) we show the interface stress, that is, the stress evaluated just above the dot/matrix interface. The location of stress evaluation is further indicated in the insets. The figures in the right column [(b), (d), and (f)] use a log-log scale to illustrate the asymptotic dependence of stress on dot depth ($\sigma_{kk} \sim h^{-3}$) for large depths.

inclusion volume is small in comparison to the matrix volume. Since the intention is to simulate a semi-infinite domain, the depth of the matrix below the deepest inclusion must be “much larger” than the thickness of the matrix separating the inclusion from the surface. For a finite-element model limited to a relatively small number of elements, this requirement becomes increasingly costly with larger quantum dot submergences. In each case, we make the depth of the overall mesh large enough that there is at least four times more matrix below the base of the inclusion than above it.

The two remaining lateral walls in the mesh for the isolated quantum dot must not reflect a symmetry between groups of four unit cells (to do so would imply an infinite two-dimensional array of submerged inclusions). Rather, we use a condition similar to that used at the bottom surface, that is, we require that the distance between the inclusion and the far lateral walls be large.

For the periodic case, symmetry was enforced with a zero normal displacement condition at all four lateral walls,

so that the elastic field within the mesh is representative of an infinite two dimensional array of submerged inclusions. The zero normal displacement condition results in a mirror image stress field, which if imposed at each lateral wall, appears as the intended inclusion array. Typical meshes included in this investigation contained between 6000 and 10 000 total elements.

IV. RESULTS AND DISCUSSION

A. Single quantum dot

We have seen how stress fields can be obtained for submerged inclusions using the point dilatation model, the mis-fitted ellipsoid model, or the finite-element cuboid and trapezoid models. Comparison of these fields is undertaken here by evaluation of the trace of the stress tensor (σ_{kk}) at three points of interest: the surface directly above the dot ($x_3 = 0$), a depth $c/2$ below the surface, where $c = V^{1/3}$, and the upper surface of the dot (at the interface between the dot and the matrix). The latter location is not shown for the point source of dilatation, since the precise interfacial position is not defined. Throughout, Poisson’s ratio is taken as $1/3$. For the ellipsoid, the aspect ratio is taken as 3, i.e., $a_1 = a_2 = 3a_3$. For the cuboid and the 30° trapezoid, the same height and volume are used as for the ellipsoid.

Figure 5(a) shows the variation of stress at the surface with inclusion depth h . As expected, the stress asymptotically approaches zero as the inclusion is moved further from the surface. The same information is shown on a log-log plot in Fig. 5(b), where it can be seen that the slope of the curves approaches -3 , indicative of the $1/h^3$ decay of stress. Moreover, the point source and ellipsoidal stresses converge as the dot exceeds 1.5 to 2 times the cube root of the volume of the ellipse c , which may be regarded as a characteristic length for this stress field. The FEM results are shown as discrete points lying quite close to the ellipsoidal stress curve.

Figures 5(c) and 5(d) show the stress component σ_{kk} at a depth $c/2$ from the surface. Again, good convergence between the ellipsoid and the point source solutions occurs as the depth of the inclusion exceeds $1.5c$ to $2c$. Both sets of finite-element results are in good agreement with the analytic results. The calculated FEM data points in all cases thus far [Figs. 5(a)–5(d)] tend to show slightly more disagreement as the depth of the dot increases. We speculate that this is tied to boundary effects, that is, artificial “image” components exist due to the four lateral faces of the mesh, as well as the bottom surface of the mesh (the latter of which is expected to dominate more for deeper inclusions), which are not manifested in the ellipsoidal or point source solutions.

Finally, in Figs. 5(e) and 5(f), we show the stress just outside of the dot as it is moved from the boundary. Interestingly, this stress component decays to zero. This result, though not intuitive, was first noted by Eshelby^{9,10} and does not hold for the other individual stress components at this location. In fact, the stress component σ_{kk} vanishes everywhere outside the ellipsoid (and the point force) in an infinite medium. The image errors mentioned earlier still apply to the FEM data points. In addition, the exact details of the shape of the inclusion should be more important here than in

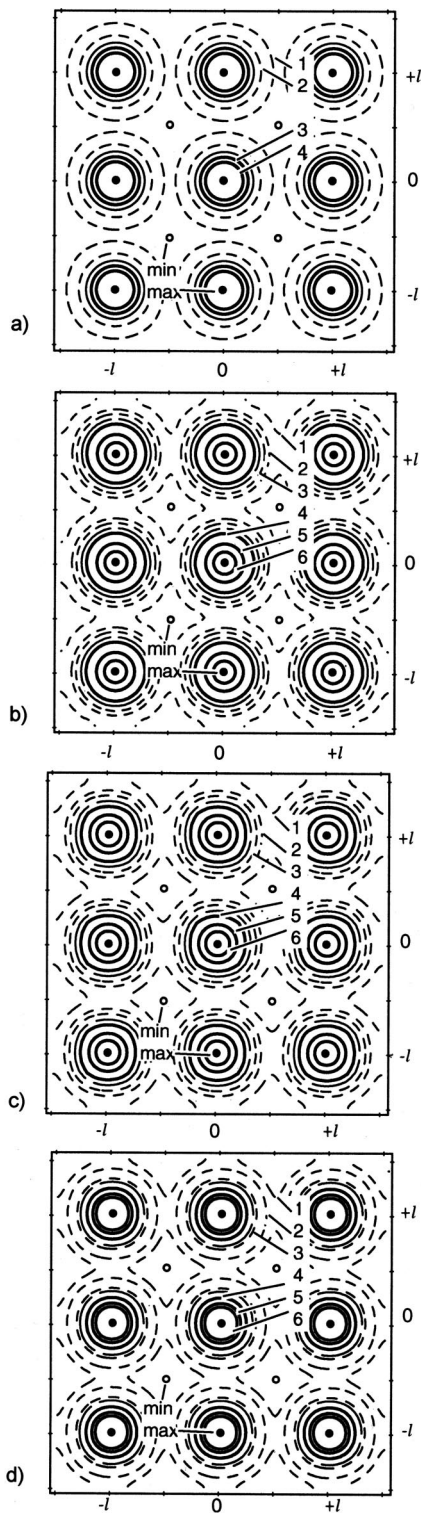


FIG. 6. Contour plots of the trace of the stress tensor at the surface σ_{kk} (in units of $f\mu$), for an array of quantum dots at depth $3a_3$ and spacing $l = 12a_3$. In all cases, positive stresses are denoted by a solid line, negative values are denoted by a dashed line, and a zero value of stress is indicated by the long dashes. (a) Array of point dilatations: values of the nonzero contours are (1) -0.3 , (2) -0.2 , (3) 0.3 , and (4) 0.8 , with a minimum of -0.31 and a maximum of 3.3 . (b) Array of ellipsoids ($a_1 = a_2 = 3a_3$): values of the nonzero contours are (1) -0.4 , (2) -0.3 , (3) -0.2 , (4) 0.3 , (5) 1.0 , and (6) 1.5 , with a minimum of -0.42 and a maximum of 1.8 . (c) Array of cuboids: values of the nonzero contours are (1) -0.38 , (2) -0.3 , (3) -0.2 , (4) 0.3 , (5) 1.0 , and (6) 1.5 , with a minimum of -0.4 and a maximum of 1.9 . (d) Array of trapezoids: values of the nonzero contours are (1) -0.29 , (2) -0.25 , (3) -0.1 , (4) 0.3 , (5) 0.7 , and (6) 1.0 , with a minimum of -0.28 and a maximum of 1.9 .

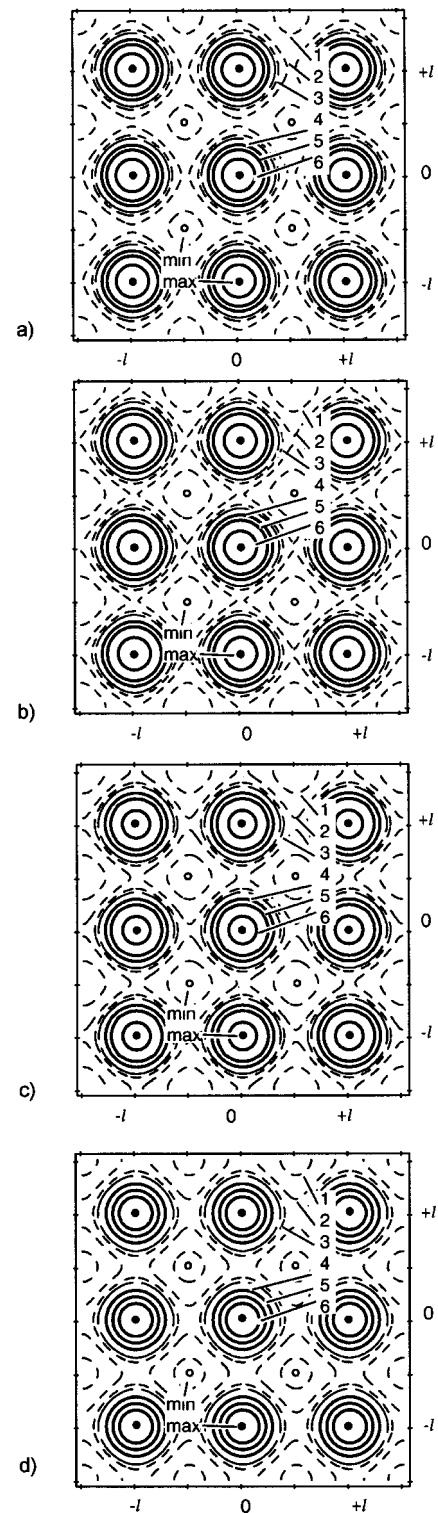


FIG. 7. Contour plots of the trace of the stress tensor at the surface σ_{kk} (in units of $f\mu$), for an array of quantum dots at depth $6a_3$ and spacing $l = 12a_3$. In all cases, positive stresses are denoted by a solid line, negative values are denoted by a dashed line, and a zero value of stress is indicated by the long dashes. (a) Array of point dilatations: values of the nonzero contours are (1) -0.1 , (2) -0.05 , (3) -0.02 , (4) 0.05 , (5) 0.1 , and (6) 0.2 , with a minimum of -0.11 and a maximum of 0.3 . (b) Array of ellipsoids ($a_1 = a_2 = 3a_3$): values of the nonzero contours are (1) -0.1 , (2) -0.05 , (3) -0.02 , (4) 0.05 , (5) 0.1 , and (6) 0.2 , with a minimum of -0.14 and a maximum of 0.28 . (c) Array of cuboids: values of the nonzero contours are (1) -0.1 , (2) -0.05 , (3) -0.02 , (4) 0.05 , (5) 0.1 , and (6) 0.2 , with a minimum of -0.13 and a maximum of 0.25 . (d) Array of trapezoids: values of the nonzero contours are (1) -0.09 , (2) -0.05 , (3) -0.02 , (4) 0.05 , (5) 0.1 , and (6) 0.15 , with a minimum of -0.1 and a maximum of 0.22 .

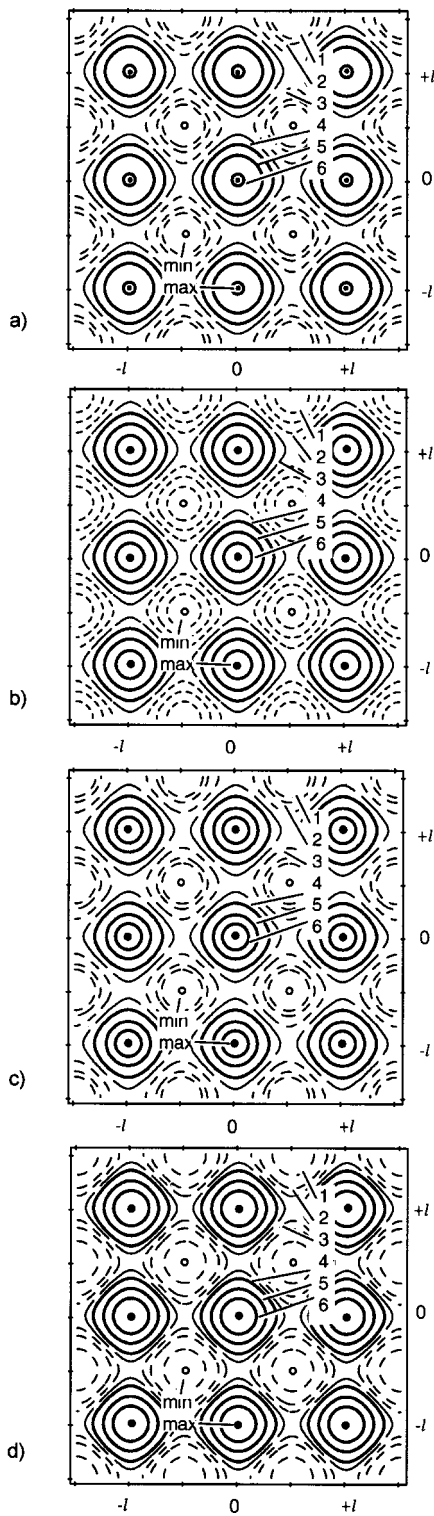


FIG. 8. Contour plots of surface stress σ_{kk} (in units of $f\mu$), for an array of quantum dots at depth $12a_3$ and spacing $l=12a_3$. In all cases, positive stresses are denoted by a solid line, negative values are denoted by a dashed line, and a zero value of stress is indicated by the long dashes. (a) Array of point dilations: values of the nonzero contours are (1) -0.005 , (2) -0.004 , (3) -0.002 , (4) 0.002 , (5) 0.005 , and (6) 0.009 , with a minimum of -0.0071 and a maximum of 0.0093 . (b) Array of ellipsoids ($a_1=a_2=3a_3$): values of the nonzero contours are (1) -0.006 , (2) -0.004 , (3) -0.002 , (4) 0.002 , (5) 0.005 , and (6) 0.008 , with a minimum of -0.0072 and a maximum of 0.0093 . (c) Array of cuboids. The values of the nonzero contours are (1) -0.005 , (2) -0.004 , (3) -0.002 , (4) 0.002 , (5) 0.005 , and (6) 0.007 , with a minimum of -0.0066 and a maximum of 0.0083 . (d) Array of trapezoids: values of the nonzero contours are (1) -0.004 , (2) -0.002 , (3) -0.001 , (4) 0.001 , (5) 0.003 , and (6) 0.005 , with a minimum of -0.0056 and a maximum of 0.0068 .

the earlier cases; therefore, it is not surprising that the trapezoid and cuboid results show a modest level of disagreement with the analytical solution.

B. Ordered array of dots

In this section we consider a square array of dots at various prescribed depths h and spacing $l=12a_3$ [see Fig. 3(b)]. We continue to use the stress trace (σ_{kk}) as a basis for comparison. Specifically, we use surface contour plots of the stress trace predicted by the point dilatation, ellipsoid, and finite-element models. These plots for the trace of the stress tensor at the surface are shown in Figs. 6–8. No evaluation was made of differences between stresses below the surface.

In Figs. 6(a)–6(d) we show stress contours for an array of dots at depth $h=3a_3$. Specific values denoted by the contours, as well as the maximum and minimum values, are given in the caption in units of $f\mu$. The extrema of the stress distribution appear directly above a given dot, as well as directly above a square quadruplet of four dots. Of all the depths we consider, the dissimilarities between all four results are most evident here, due to the close proximity of the dots to the surface. Moreover, we note the symmetry of the stress distributions due to the point dilatation and the ellipse are of a circular nature, while for the cuboid and trapezoid, the perfect circular symmetry is slightly broken. In other words, the contours reflect the shape of the particular dot. As the dot moves closer to the surface, we expect this feature to become more dominant.

In Fig. 7 the corresponding results are shown for an array of dots at depth $h=6a_3$. There is moderate quantitative agreement between all four models, indicating that the precise shape of the dot is a much less important factor at this depth. In addition, elements of a square-like symmetry begin to appear in the stress distribution at locations removed from the point directly above any given dot. Moreover, this square-like motif in the stress contours is rotated by 45° with respect to the original square lattice of dots.

Finally, in Fig. 8, the results are shown for an array of dots at depth $h=12a_3$. A square-like symmetry to the stress distribution (also rotated by 45°), similar to the previous case, is more pervasive. The quantitative level of agreement is good, but not nearly as good as expected for this depth. Several sources of error can be identified that can explain the disagreement: in the FEM results, no image contributions are expected from the lateral walls of the mesh, since the periodic nature of the geometry is perfectly captured. However, the image error from the bottom surface is expected to be most prevalent at this depth than in the earlier cases. In addition, the number of terms needed for the sums in Eq. (3) to obtain good convergence (applicable to the point of dilatation and ellipsoid arrays) became exceedingly large when h is greater than $\sim 10a_3$, and accordingly, we are confident of the results in Figs. 8(a) and 8(b) only to within about $\pm 5\%$.

V. SUMMARY

We conclude that over a wide range of geometries, simple analytical models based on ellipsoids, or to some extent based on point dilatations, may be the most efficient

means of obtaining reasonable estimates of the elastic stresses associated with quantum dots. In particular, the finite-element models described in this article very closely matched the predictions of the ellipsoidal inclusion model in the isolated and periodic cases. This close correspondence between the analytical ellipsoid and the FEM cuboid/trapezoid persists to remarkably shallow submergence depths, indicating a potentially high usefulness in modeling typical three-dimensional dot array geometries.

The exception to the close match of ellipsoid and finite-element models is the case of predicted stresses at the upper interface between the dot and the matrix. The interface lies in a region characterized by large stress gradients, which would have an expected detrimental effect on the accuracy of the finite-element models. However, even with an exceptionally fine mesh, differences in modeled dot shape should be expected to give rise to variations in predicted stress values at the interface. These differences would be attributed both to variations in interface depth and to differences in local stress concentrations at the top center interface of dots of different shape.

Of perhaps more use to the modeler of SAQD systems is that only one “primary” dot (or region associated therewith) should be considered in detail, while all other dots may be approximated as ellipsoids or point sources.

Finally, we note that the calculations in this article clearly show that quantum dots either on the free surface or near the free surface lead to large hydrostatic stresses and strains in the matrix. The hydrostatic strain will lead to changes in both the conduction and valence band levels. We believe that this effect should be included in the treatment of the matrix electronic properties for near surface dots and stressors.

ACKNOWLEDGMENTS

This work was supported by the AFOSR Award (Dr. Dan Johnstone, Contract Monitor). A.E.R. was supported in part by Grant No. 97-3006 from the Russian Research Council “Physics of Solid Nanostructures.”

¹D. Leonard, K. Pond, and P. Petroff, *Phys. Rev. B* **50**, 11687 (1994).

²A. Zunger, *MRS Bull.* **23**, 15 (1998).

³D. Bimberg, M. Grubdmann, and N. N. Ledentsov, *MRS Bull.* **23**, 31 (1998).

⁴S. Rouvimov, Z. Liliental-Weber, W. Swider, J. Washburn, E. R. Weber, A. Sasaki, A. Wakahara, Y. Furukawa, T. Abe, and S. Noda, *J. Electron. Mater.* **27**, 427 (1998).

⁵Q. Xie, A. Madhukar, P. Chen, and N. P. Kobayashi, *Phys. Rev. Lett.* **75**, 2542 (1995).

⁶V. A. Shchukin, N. N. Ledentsov, P. S. Kop'ev, and D. Bimberg, *Phys. Rev. Lett.* **75**, 2968 (1995).

⁷J. Tersoff, C. Teichert, and M. G. Lagally, *Phys. Rev. Lett.* **76**, 1675 (1996).

⁸V. A. Shchukin, D. Bimberg, V. G. Malyshekin, and N. N. Ledentsov, *Phys. Rev. B* **57**, 12262 (1998).

⁹Y. W. Zhang, S. J. Xu, and C.-H. Chiu, *Appl. Phys. Lett.* **74**, 1809 (1999).

¹⁰A. E. Romanov, P. M. Petroff, and J. S. Speck, *Appl. Phys. Lett.* **74**, 2280 (1999).

¹¹H. Lee, J. A. Johnson, J. S. Speck, and P. M. Petroff, *J. Vac. Sci. Technol.* (to be published).

¹²F. Jónsdóttir and L. B. Freund, *Mech. Mater.* **20**, 337 (1995).

¹³T. R. Mattsson and H. Metiu, *Appl. Phys. Lett.* **75**, 926 (1999).

¹⁴M. Grundmann, O. Stier, and D. Bimberg, *Phys. Rev. B* **52**, 11969 (1995).

¹⁵H. Jiang and J. Singh, *Physica E (Amsterdam)* **2**, 614 (1998).

¹⁶J. H. Davies, *J. Appl. Phys.* **84**, 1358 (1998).

¹⁷J. Groenen, C. Priester, and R. Carles, *Phys. Rev. B* **60**, 16013 (1999).

¹⁸J. H. Davies, *Appl. Phys. Lett.* **75**, 4142 (1999).

¹⁹J. A. Barker and E. P. O'Reilly, *Phys. Rev. B* **61**, 13840 (2000).

²⁰J. D. Eshelby, *Proc. R. Soc. London, Ser. A* **241**, 376 (1957).

²¹J. D. Eshelby, *Proc. R. Soc. London, Ser. A* **252**, 561 (1959).

²²J. R. Downes, D. A. Faux, and E. P. O'Reilly, *J. Appl. Phys.* **81**, 6700 (1997).

²³A. D. Andreev, J. R. Downes, D. A. Faux, and E. P. O'Reilly, *J. Appl. Phys.* **86**, 297 (1999).

²⁴G. S. Pearson and D. A. Faux, *J. Appl. Phys.* **88**, 730 (2000).

²⁵T. Benabbas, P. François, Y. Androussi, and A. Lefebvre, *J. Appl. Phys.* **80**, 2763 (1996).

²⁶A. Ponchet, D. Lacombe, L. Durand, D. Alquier, and J.-M. Cardonna, *Appl. Phys. Lett.* **72**, 2984 (1998).

²⁷T. Benabbas, Y. Androussi, and A. Lefebvre, *J. Appl. Phys.* **86**, 1945 (1999).

²⁸G. Muralidharan, *Jpn. J. Appl. Phys., Part 2* **39**, L658 (2000).

²⁹W. Yu and A. Madhukar, *Phys. Rev. B* **79**, 905 (1997).

³⁰C. Pryor, J. Kim, L. W. Wang, A. J. Williamson, and A. Zunger, *J. Appl. Phys.* **83**, 2548 (1998).

³¹M. E. Bachlechner, A. Omeltchenko, A. Nakano, R. K. Kalia, P. Vashishta, I. Ebbsjö, A. Madhukar, and P. Messina, *Appl. Phys. Lett.* **72**, 1969 (1998).

³²Y. P. Chiu, *J. Appl. Mech.* **44**, 587 (1977).

³³Y. P. Chiu, *J. Appl. Mech.* **45**, 302 (1978).

³⁴T. Mura, *Micromechanics of Defects in Solids* (Martinus Nijhoff, Boston, 1987).

³⁵K. Seo and T. Mura, *J. Appl. Mech.* **46**, 568 (1979).

³⁶J. P. Hirth and J. Lothe, *Theory of Dislocations* (Wiley, New York, 1982).

³⁷R. De Wit, *Solid State Phys.* **10**, 249 (1960).

³⁸R. D. Mindlin and D. H. Cheng, *J. Appl. Phys.* **21**, 931 (1950).

³⁹J. C. M. Li, *Metall. Trans. A* **9A**, 1353 (1978).

⁴⁰K. L. Malyshev, M. Yu. Gutkin, A. E. Romanov, A. A. Sitnikova, and L. M. Sorokin, *Sov. Phys. Solid State* **30**, 1176 (1988).

⁴¹V. I. Vladimirov, M. Yu. Gutkin, and A. E. Romanov, *Mech. Composite Mater.* **3**, 450 (1987).

⁴²B. Michel, *Arch. Mech.* **32**, 73 (1980).

⁴³F. Loges, B. Michel, and A. Christ, *Z. Angew. Math. Mech.* **65**, 65 (1985).